Presampler scale studies using electrons from Z boson decays.

Klitos Savva

Supervised by: Dr. Otilia Ducu & Guillaume Unal

European Laboratory for Particle Physics, CERN

August 27, 2021

E-mail: klitos.savva@cern.ch

The Project

A precise calibration of energy measurement of photons and electrons plays a crucial role in various precision measurements carried out in ATLAS, such as the Higgs boson mass and couplings measurements in the di-photon channel or for a precise measurement of the W boson mass. One of the key inputs to the energy regression algorithm, is an estimate of the energy lost by electrons and photons when interacting with passive volumes of the detector before reaching the calorimeter (e.g. inner detector, cryostat walls, etc). This estimate is provided by the presampler, an active layer of liquid argon positioned in front of the electromagnetic calorimeters. The project is focusing on the in situ calibration of the presampler energy scale using electrons from Z boson decays recorded in LHC Run 2 data.

The results were presented in Egamma group meetings:

1. 12/07/2021; PS scale with electrons; Egamma Calibration Sub-group Meeting
2. 26/08/2021; PS scale with electrons; Egamma Calibration Sub-group Meeting
3. 26/08/2021; PS scale with electrons; Egamma Plenary Meeting

Contents

---

1 ATLAS Detector

At the Large Hadron Collider (LHC), a range of detectors are being used in different experiments to investigate and analyse the myriad of particles produced by collisions in the accelerator [1]. ATLAS and CMS are the largest two experiments which are using general-purpose detectors to investigate the largest range of physics possible, from the search for the Higgs boson to particles that could make up dark matter [2].

Around the LHC, beams of protons are being accelerated which collide at the centre of the ATLAS detector. These collisions lead to the production of debris in the form of particles which disperse out from the collision point in all directions. The design goal of the ATLAS detector is to be able to detect even the most tiny, short-lived and energetic of these particles. To materialise this, the detector consists of six different detecting subsystems which are arranged concentrically in layers around the collision point. The design of ATLAS permits the recording of the trajectories, the momenta and the energy of particles simultaneously enabling individual particle measurement and identification. A schematic of the ATLAS detector is shown in Figure 1.

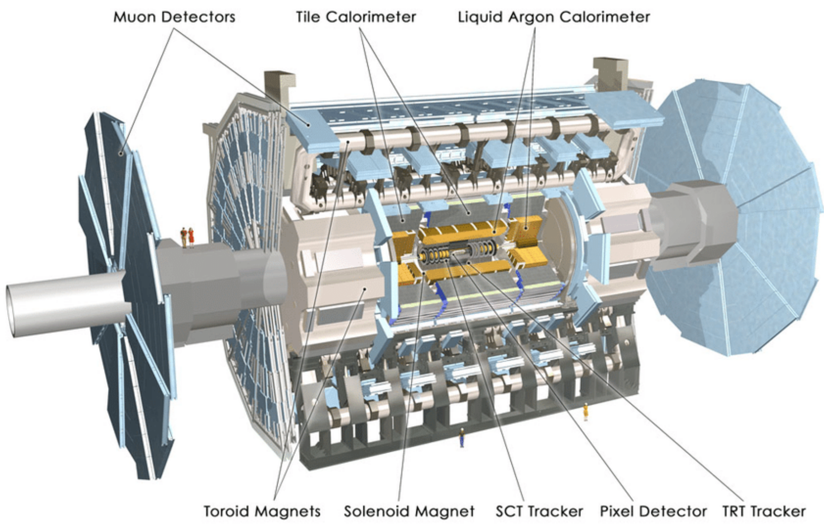

Figure 1: Schematic of the ATLAS detector as extracted from [3]. A precise measurement of the momenta is fasciliated via a magnet system bending the path of charged particles.

In the following text, the main components of the ATLAS detector will be explored. Namely, the inner detector, the calorimeters, and the muon spectrometer.

Inner Detector (ID)

A precise reconstruction of tracks within a pseudorapidity range $|\eta| \leq 2.5$, is provided via the inner tracking detector. As indicated by Figure 1, the innermost part of the ID is a pixel detector (silicon) providing three measurement points for charged particles whose origin is the beam-interaction region. The pixel detector is surrounded by a semiconductor tracker (SCT) which is surrounded by a transition radiation tracker (TRT) transition radiators. The ID enables an accurate transverse momentum measurement and reconstruction of tracks from the primary proton-proton collision region [5].

Calorimeters

The energy of electrons and photons upon interaction with matter is measured using electromagnetic calorimeters whereas the energy of hadrons is being sampled using hadronic calorimeters upon their interaction with atomic nuclei. Calorimeters can stop most known particles with the exception of muons and neutrinos. The components of the ATLAS calorimetry system are: the Liquid Argon **(LAr)** Calorimeter and the Tile Hadronic Calorimeter. A cut-away view of the calorimeter system is shown in Figure 2.

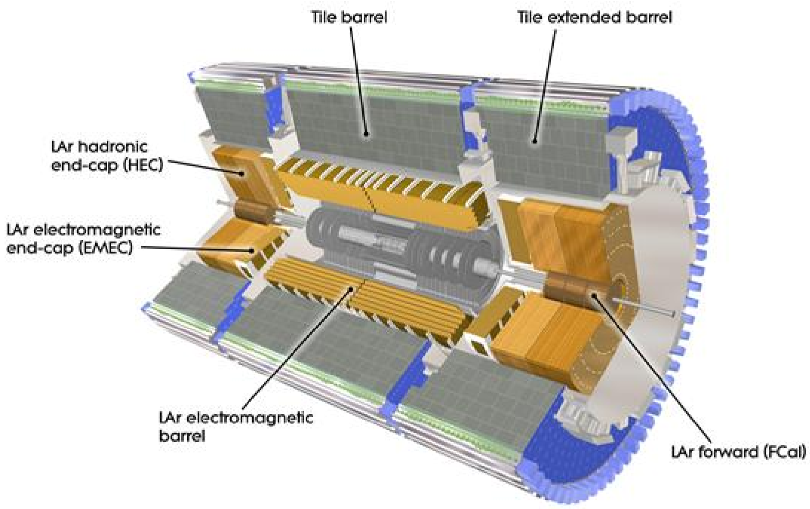

Figure 2: Cut-away view of the ATLAS calorimeter system as extracted from [6].

LAr Calorimeter

The inner detector is surrounded by a high-granularity liquid argon electromagnetic calorimeter. The multi-layered metal (lead) structure of the LAr leads to the creation of particle showers which upon ionising the liquid argon sandwiched between the layers lead to the production of a measurable electric current. The purpose of its accordion structure (honeycomb pattern) is to ensure that no particle escapes unchallenged.

The LAr calorimeter enables the measurement of the energy and position of the electromagnetic (EM) showers with $|\eta| < 3.2$. This EM calorimeter is divided into different sections with those being; a barrel section and two end-cap sections. The barrel covers the pseudorapidity region $|\eta| < 1.475$ whereas the end-caps cover the region $1.375 < |\eta| < 3.2$. For $|\eta| < 2.5$, the calorimeter is composed of three sampling layers. The characteristics of the first sampling layer are summarised in Table 1.

Layer 1				
Thickness	$4.4\ X_0$ (Radiation Lengths)			
Pseudorapidity Regions	$\eta < 1.4$	$1.5 < \eta < 2.4$	$1.4 < \eta < 1.5$	$2.4 < \eta < 2.5$
Typical Cell Size ($\Delta\eta \times \Delta\phi$)	0.003×0.0982 (Barrel)		0.025×0.0982	

Table 1: Summary of the characteristics of the first layer of the ATLAS EM calorimeter, reproduced from [5].

The first layer of the calorimeter has a fine η granularity which enables the event-by-event discrimination between single photon showers and two overlapping showers originating from neutral hadron decays for transverse momenta up to 0(100 GeV) in the pseudorapidity region $|\eta| < 1.37$ or $1.52 < |\eta| < 2.37$. In contrast, the energy deposited by photon and electron showers is collected by the second sampling layer whose characteristics are summarised in Table 2.

The correction for high-energy showers leaking out of the calorimeter is provided by the third sampling layer which has a depth of circa $2\ X_0$ and granularity of 0.05×0.0245 ($\Delta\eta \times \Delta\phi$). In addition to the accordion calorimeter, a presampler layer is present in front of the

Layer 2	
Thickness	17 X_0 (Radiation Lengths)
Typical Cell Size (Granularity) ($\Delta\eta \times \Delta\phi$)	0.025×0.0245

Table 2: Characteristics of the second layer of the ATLAS EM calorimeter, reproduced from [5].

calorimeter. The purpose of this layer is to provide a correction for the energy loss upstream of the calorimeter. Similarly to the first sampling layer, the presampler has a granularity of 0.025×0.0982 ($\Delta\eta\times\Delta\phi$) and is equipped with an active layer of LAr. This active layer has a thickness of 1.1 cm in the barrel and 0.5 cm in the end-caps. The approximated thicknesses of upstream material are summarised in Table 3 and a sketch of a barrel module is shown in Figure 3.

Pseudorapidity Region	Thickness (Radiation Lengths)
$\|\eta\| < 0.6$	2 X_0
$0.6 < \|\eta\| < 0.8$	2-3 X_0 (linear increase)
$0.8 < \|\eta\| < 1.8$	≈ 3 X_0
$\|\eta\| = 1.7$	5-6 X_0 (barrel end-cap transition region)

Table 3: Summarised thicknesses of material upstream of the presampler, reproduced from [5].

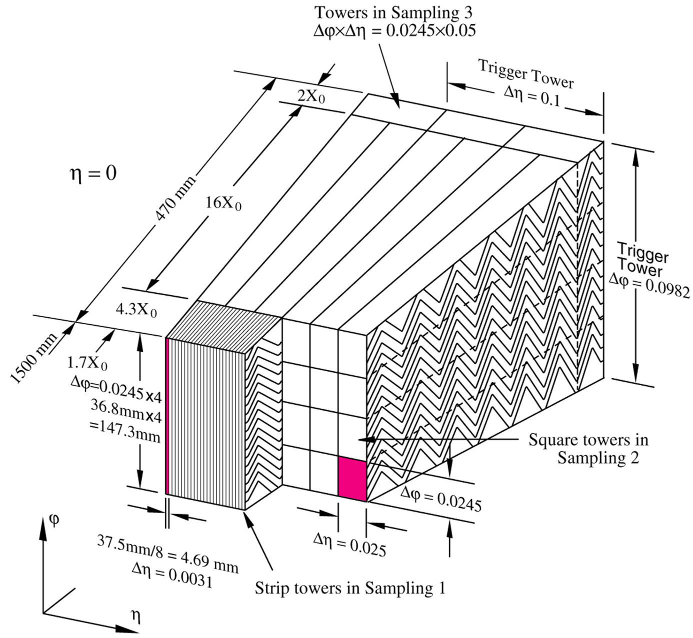

Figure 3: Schematic of the barrel module of the ATLAS electromagnetic calorimeter. This was extracted from [7].

Hadronic Calorimeter

The ATLAS EM calorimeter is surrounded by a hadronic calorimeter. In the pseudorapidity region $|\eta| < 1.7$ this calorimeter consists of an iron-scintillator tile calorimeter whereas the regions $1.5 < |\eta| < 3.2$ (end-cap) and $3.1 < |\eta| < 4.9$ (forward) are sampled using LAr calorimeters with copper and tungsten absorbers.

Last but not least, the ATLAS EM and hadronic calorimeters are surrounded by a muon spectrometer. It is also crucial noting that an enormous amount of particle interactions ($\approx 10^9$) take place in the ATLAS detector every second. This vast flow of data is filtered through an advanced "trigger" system which tell the detector which events to record and which to ignore [4]. In fact, only one in a million collisions are flagged by the trigger system and recorded for further study.

2 Method

2.1 Overview

This chapter will introduce the relevant theory for the determination of the presampler scale using electrons.

2.2 Presampler Scale Determination

The ratio of the PS energies in data and Monte Carlo simulation is used to define the PS energy scale and is estimated using electrons originating from Z-boson decays. However, this energy ratio cannot be directly interpreted in terms of an energy scale due to approximations regarding passive material in the simulation. The effects of these approximations must be accounted as they could potentially bias the predicted PS energy distributions compared to data, thus affecting the energy scale [8].

The ratio of the energy deposited in the front (Layer 1) and middle (Layer 2) sampling layers of the calorimeter can be utilised to correct passive material effects. This $E_{1/2}$ quantity is utilised due to its high sensitivity to amounts of material upstream of the calorimeter. For instance, if there is a deficit of material in the simulation compared to data, a shower would develop earlier in data leading to a larger energy deposit in Layer 1 compared to the simulation. When there is an excess of material in simulation, then $E_{1/2}$ would be larger in MC with respect to data. However, prior to using $E_{1/2}$ to correct for upstream material, various factors have to be considered [8], [9].

The first factor that needs to be considered is the correlation between the PS energy and $E_{1/2}$ at a given pseudorapidity η. This correlation is assessed by finding a correlation factor A(η). In addition, any material mis-modelling between data and MC for which PS is not sensitive, needs to be corrected. A correction factor $b_{1/2}$ is used to account for any mis-modelling [9].

The following linear parametrisation is used to compute expected PS energy ($\mathrm{E}_0^{corr}(\eta)$) in MC upon correcting for any material-induced bias [8]

$$\frac{E_0^{corr}(\eta)}{E_0^{nom}(\eta)} = 1 + A(\eta)\left(\frac{E_{1/2}^{data}(\eta)}{E_{1/2}^{nom}(\eta)b_{1/2}(\eta)} - 1\right) \tag{2.1}$$

where A(η) and b$_{1/2}$(η) are as previously defined.

Once E$_0^{corr}$(η) is computed, the PS scale can be obtained using

$$\alpha_{PS}(\eta) = \frac{E_0^{data}(\eta)}{E_0^{corr}(\eta)} \tag{2.2}$$

2.2.1 Error Propagation

The associated uncertainty to the $\alpha_{PS}(\eta)$ is computed by re-arranging equations 2.1 & 2.2 and employing standard error propagation techniques as outlined in equations 2.3 - 2.9.

$$\Gamma = \frac{E_{1/2}^{data}(\eta)}{E_{1/2}^{nom}(\eta)} \tag{2.3}$$

$$\Delta\Gamma = \Gamma \times \left(\left(\frac{\Delta E_{1/2}^{data}(\eta)}{E_{1/2}^{data}(\eta)} \right)^2 + \left(\frac{\Delta E_{1/2}^{nom}(\eta)}{E_{1/2}^{nom}(\eta)} \right)^2 \right)^{1/2} \tag{2.4}$$

$$\Theta = \frac{E_0^{data}(\eta)}{E_0^{nom}(\eta)} \tag{2.5}$$

$$\Delta\Theta = \Theta \times \left(\left(\frac{\Delta E_0^{data}(\eta)}{E_0^{data}(\eta)} \right)^2 + \left(\frac{\Delta E_0^{nom}(\eta)}{E_0^{nom}(\eta)} \right)^2 \right)^{1/2} \tag{2.6}$$

$$\Delta AB = \left((\Delta A(\eta)^2) + (\Delta b_{1/2}(\eta))^2 \right)^{1/2} \tag{2.7}$$

$$\Delta E_0^{corr}(\eta) = \left(((\Gamma - 1) \times \Delta AB)^2 + (A(\eta) \times \Delta\Gamma)^2 \right)^{1/2} \tag{2.8}$$

$$\Delta\alpha_{PS}(\eta) = \alpha_{PS}(\eta) \times \left(\left(\frac{\Delta\Theta}{\Theta} \right)^2 + \left(\frac{\Delta E_0^{corr}(\eta)}{E_0^{corr}(\eta)} \right)^2 \right)^{1/2} \tag{2.9}$$

2.3 Upstream Material Correction A(η) Determination

As discussed in section 2.2, the correlation factor A(η) needs to be obtained prior to computing the PS scale. This factor can be estimated from relative variations of PS energy deposits (E_0) and the corresponding variation in $E_{1/2}$ in MC samples with distorted geometries as a function of pseudorapidity [8].

To obtain A(η), ratios of the profiles of E_0 and $E_{1/2}$ are plotted for the different distorted geometries and fitted using equation 2.1. The profiles are being fitted while fixing the $b_{1/2}$ correction to 1. This is being done to ensure that the MC sample with nominal geometry will not be corrected. In addition, MC samples with geometry configurations with material only added between the PS and the accordion should be neglected from the fit as these will only cause a shift in $E_{1/2}$ leaving E_0 unaffected. The correction factor $A(\eta)$ can then be obtained from the slope of the afforementioned linear fit [8].

According to [8], a fixed cut electron identification was used for run-1. For run-1, no material corrections being applied to the nominal geometry were ensured by fixing $b1/2$ to 1. However for run-2, a likelihood-based electron identification was used which resulted in a disagreement in $A(\eta)$ for the two runs. This was resolved by floating $b_{1/2}$ for run-2 which utilised the likelihood-based identification whilst $A(\eta)$ for run-1 (cut-based identification) was obtained by fixing $b_{1/2}$ to 1. The estimated values for $A(\eta)$ extracted from [8] are shown in Table 4.

η region	A(η) run-1	A(η) run-2	A(η) - 2013	Comment
$0.0 < \|\eta\| < 0.8$	2.48 ± 0.09	2.51 ± 0.07	2.48 ± 0.09	[8]
$0.8 < \|\eta\| < 1.37$	1.65 ± 0.05	1.85 ± 0.06	1.65 ± 0.05	[8]
$1.37 < \|\eta\| < 1.52$	-	-	1.65 ± 0.05	[9]
$1.55 < \|\eta\| < 1.8$	1.59 ± 0.09	1.5 ± 0.1	-	[8]

Table 4: Average A(η) in different η regions.

2.4 $E_{1/2}$ Intercalibration Correction $b_{1/2}$

As discussed in section 2.2, $b_{1/2}$ is used to correct for material-mismodelling between data and MC for which the energy deposits in the PS are unaffected. In other words in the parametrisation (Equation 2.1), $b_{1/2}$ offsets the linear correlation between E_0 and $E_{1/2}$ since any material after the PS will induce shifts only in $E_{1/2}$. The fitted values used in [8] are shown in Figure 4.

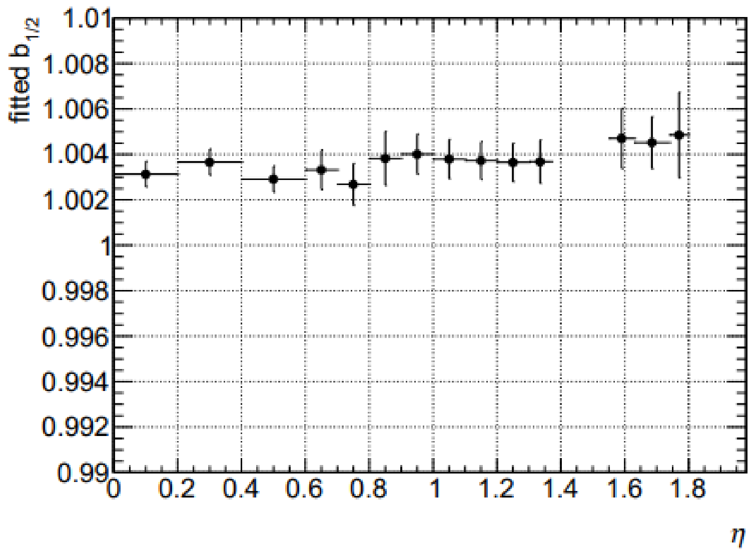

Figure 4: Fitted values of $b_{1/2}$ as extracted from [8].

3 Data and Simulated MC

3.1 Overview

This chapter will introduce and provide a description of the datasets used for the computation of the PS scale.

3.2 Datasets

As discussed in section 2.2, the PS scale is computed based on electrons from Z boson decays. For this study, the data samples are derived from the LHC Full Run-2 which has an integrated luminosity (L_{int}) of 139 fb^{-1}. However, out of the full run-2 data, only data taken in 2017 are used (L_{int} = 44.3 fb^{-1}). To compare theory with real data, simulated data (MC) are used in LHC experiments. The process of conduction a full simulation is summarised in Table 5.

Step	Description
Event Generation	Programs relying on theoretical predictions, experimental inputs and phenomenological models are used to generate hadronic final states from proton-proton collisions
Detector Simulation	Simulation of interactions of generate particles inside the ATLAS detector
Digitisation	Particle interactions are being used to derive the detector response which is written in a compatible format with the real output of the detector. Realistic experimental background can be created by piling-upseveral simulated events
Reconstuction	Reconstruction of particle trajectories and energies from the detector

Table 5: Summary of the steps required to conduct a full MC simulation (ATLAS) [10].

However, an agreement between real data and simulated data is not always present. A disagreement could be present due to the conditions not being exactly the same (energy, pileup). Omitting background processes in the simulated or the mismodelling of physics by the theory could lead also to a disagreement [10]. The simulated sample used in this study is named mc16d and it is derived in such a way as to avoid the afforementioned reasons leading to a lack of agreement between real and simulated data. This sample is derived from large samples of $Z \rightarrow ee$ events generated with POWHEG interfaced with PYTHIA and reweighed with pileup profiles matching those of 2017. In addition, certain constraints are imposed on the selected electrons which are summarised in Table 6.

Quantity	Criteria	Comments
Transverse Momentum (p_T)	$p_T > 27$ GeV	Applied at trigger level
Pseudorapidity ($\|\eta\|$)	$\|\eta\| < 2.47$	Applied at ntuple production step
Invariant Mass ($m_{e^+e^-}$)	80 GeV $< m_{12} <$ 100 GeV	Applied at plot production step

Table 6: Summary of the criteria for selecting electrons.

4 Preliminary Tests

4.1 Overview

This section will introduce the preliminary tests which were conducted. These tests were conducted to investigate any selection criteria applied at a trigger level or at the ntuple production step while also comparing real and simulated data.

4.2 Invariant Mass of the electron-positron pair, $m_{e^+e^-}$

Invariant Mass of the electron-positron pair $m_{e^+e^-}$ was one of the initial quantities to be tested. A normalised to unity histogram of $m_{e^+e^-}$ from real data and simulated data was plotted to test the quantity and is shown in Figure 5.

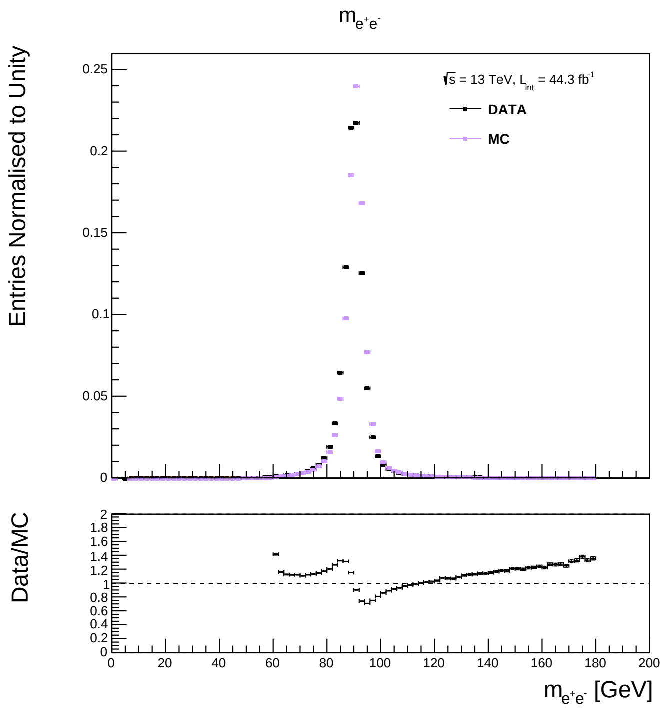

Figure 5: Plot of the invariant mass for data and MC. The bottom plot shows the ratio of the two different datasets.

From Figure 5, it is clear that a selection criterion was not applied at the ntuple production step for the datasets. Therefore, a selection criterion requiring $m_{e^+e^-}$ to be in the range of 80 GeV to 100 GeV was applied at the plot production step since this study is based on electrons from neutral Z boson decays which has a rest mass of circa 91 GeV.

4.3 Electron Transverse Momentum (p_T)

The selection criteria applied on the transverse momenta of the decayed electrons were investigated similarly to the invariant mass and the corresponding histograms are shown in Figure 6.

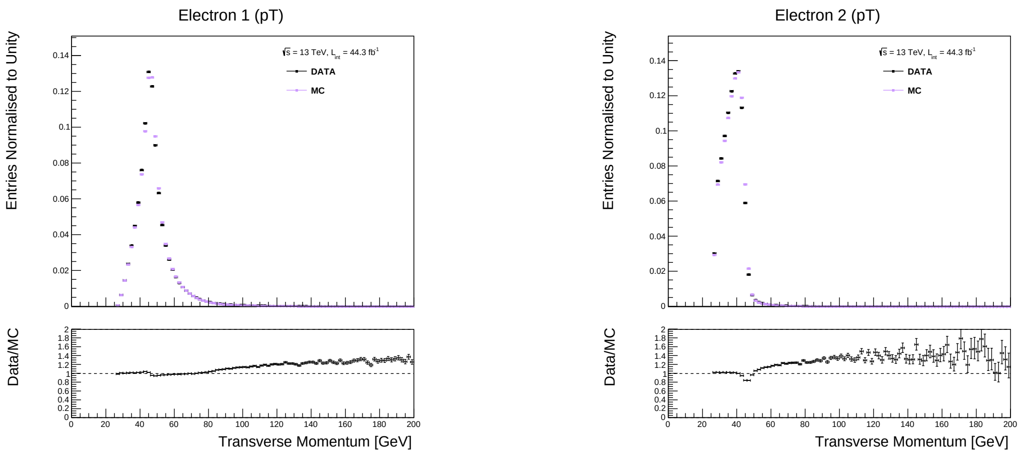

Figure 6: (a) Leading electron p_T for data and MC (b) Equivalent plot for the second electron.

Figure 6 shows the distributions of both decayed electrons peaking at circa 45 GeV as expected since the invariant mass of the decay corresponds to the mass of the Z boson. In addition, there is a good agreement between data and MC for the energy region 30 GeV to 80 GeV while the deviation in the tails should not be alarming as they will not impact the analysis due to the few statistics in the region. It is evident that a selection criterion has been imposed p_T on both the datasets as summarised in Table 6.

4.4 Electron Pseudorapidity Distribution (η)

The last criterion on applied on the decayed electrons was regarding their pseudorapidity. This was investigate in a similar manner to the invariant mass and transverse momenta and the corresponding histograms are shown in Figure 7.

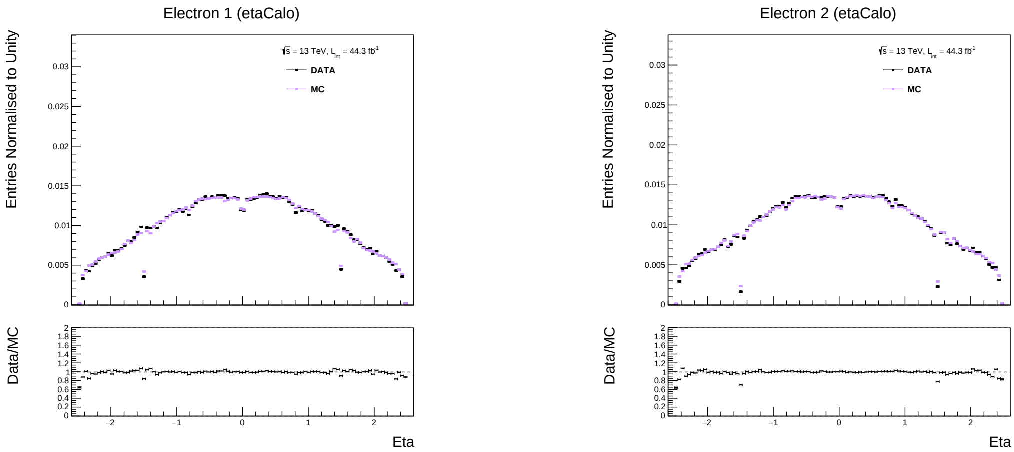

Figure 7: (a) Pseudorapidity distribution of the leading electron for data and MC (b) Equivalent plot for the second electron.

From Figure 7, a good agreement between real data and simulated data can be deduced suggesting that no background estimation is needed. In addition, the selection criterion on the pseudorapidity (6) is also verified.

4.5 End-cap (EC) High Voltage (HV) Problem

In ATL-COM-PHYS-2017-760 internal note [8], unexpected behaviour in the end-cap bin was observed compared to run-1 upon the application of a PS veto. This discrepancy between data and MC increased which was not expected since no material had been added in that region. This problem was later traced back to wrong interpretation of high voltage mapping in the end-cap. To investigate whether this problem had been resolved in the 2017 dataset plots of $\eta - \phi$ distribution were constructed for both real data and MC.

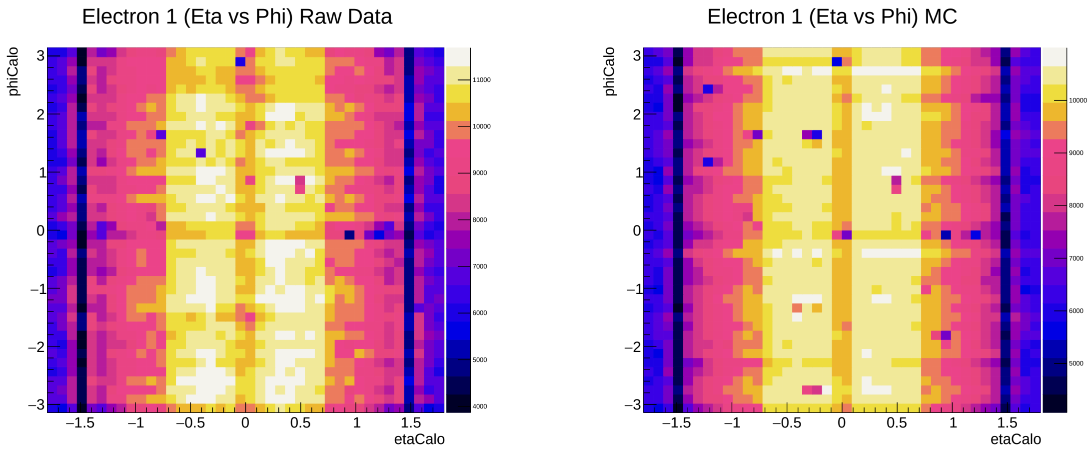

Figure 8: (a) Map of the $\eta - \phi$ distribution for the 2017 dataset (b) Equivalent map for the MC dataset (mc16d).

Figure 8 shows a smooth $\eta - \phi$ distribution for both datasets which seem to be in agreement revealing that the EC HV problem has been resolved.

4.6 Electron Raw Cluster Energy Distributions

A preliminary test was also conducted on the raw cluster energies deposited in the PS (E_0), layer 1 (E_1) and layer 2 (E_2) of the ATLAS calorimeter. These distribution were compared to the simulated distribution through normalised to unity histograms that are shown in Figure 9.

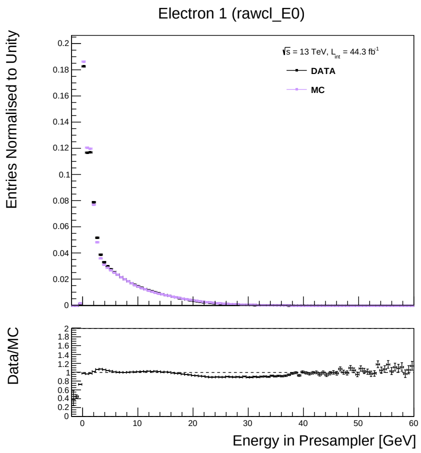

(a)

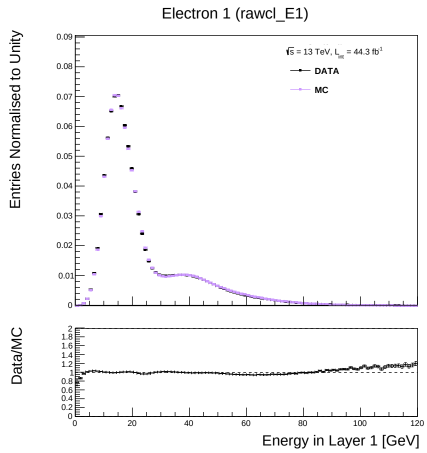

(b)

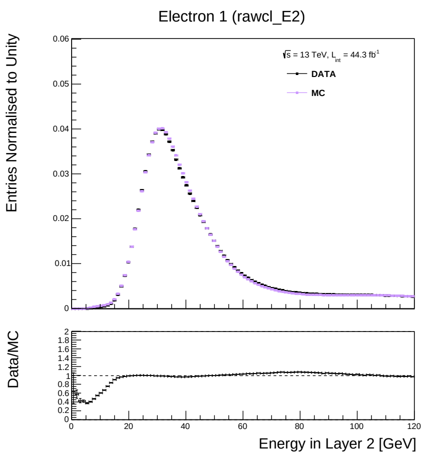

(c)

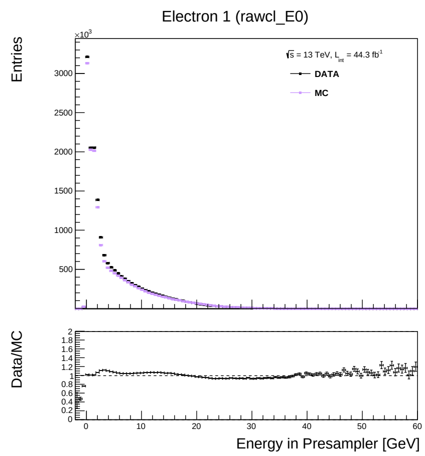

(d)

Figure 9: (a) Leading electron raw cluster energy deposited in PS for data and MC (b) Equivalent plot for energy deposited in layer 1 (c) Equivalent plot for energy deposited in layer 2. (d) Leading electron raw cluster energy deposited in PS (No Normalisation to Unity).

Plot (a) of Figure 9 indicates that there is small discrepancy (< 10 %) between real data and simulated data in the PS for the energy region 18 GeV to 38 GeV. By inspecting plot (b), a shoulder is present in the deposited energy distribution in Layer 1 at around 30 GeV. Plot (c) of Figure 9 shows a small discrepancy for energy deposited in layer 2 between data and MC for the region 0 GeV to 15 GeV. A good overall agreement between real data (2017 dataset) and simulated data (mc16d) is observed in all other energy regions of the three calorimeter layers.

The possible origin of the shoulder in the deposited energy distribution in layer 1 is further investigated by plotting histograms of the deposited energies in the barrel and end-cap regions instead of the full pseudorapidity coverage of layer 1. These plots are shown in Figure 10.

By inspecting Figure 10, the shoulder seems to be only present in the negative and positive end-cap regions. This could be attributed to the amount of material in the end-cap region since the same behaviour is observed in both end-caps. It is also worth noting that a small shoulder is present at 10 GeV in the negative EC which is not present in the positive EC.

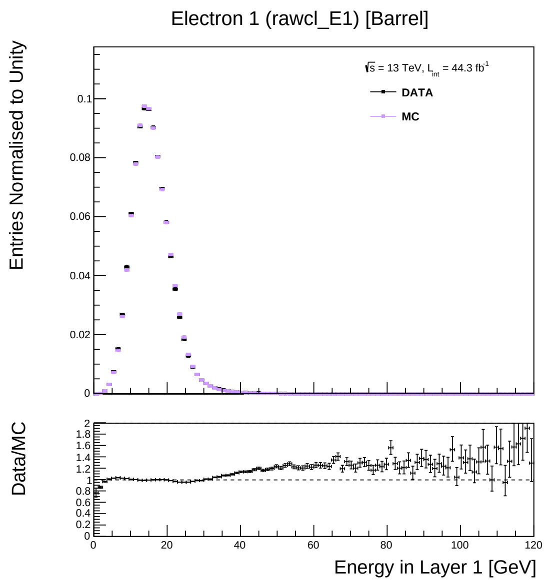

(a)

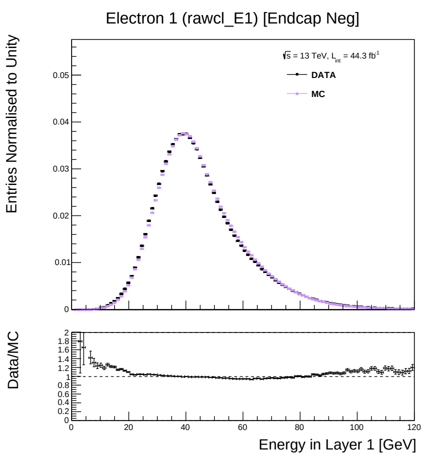

(b)

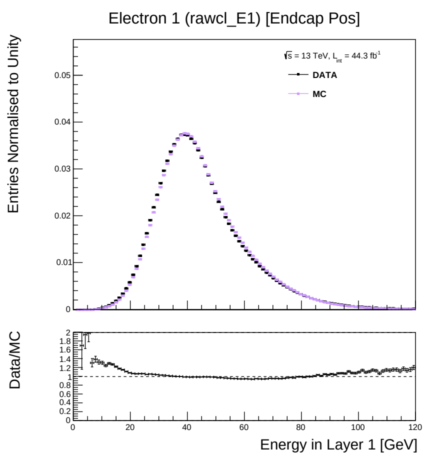

(c)

Figure 10: (a) Leading electron raw cluster energy deposited in the barrel of layer 1 (b) Equivalent plot for energy deposited in the negative end-cap region (c) Equivalent plot for energy deposited positive end-cap region.

4.7 Electron Raw Energy Distributions vs η

The concluding preliminary test conducted involved the raw cluster energy distributions for each layer as a function of pseudorapidity. This was performed by plotting profiles of the energy deposits in the layers and pseudorapidity (η) which are shown in Figure 11.

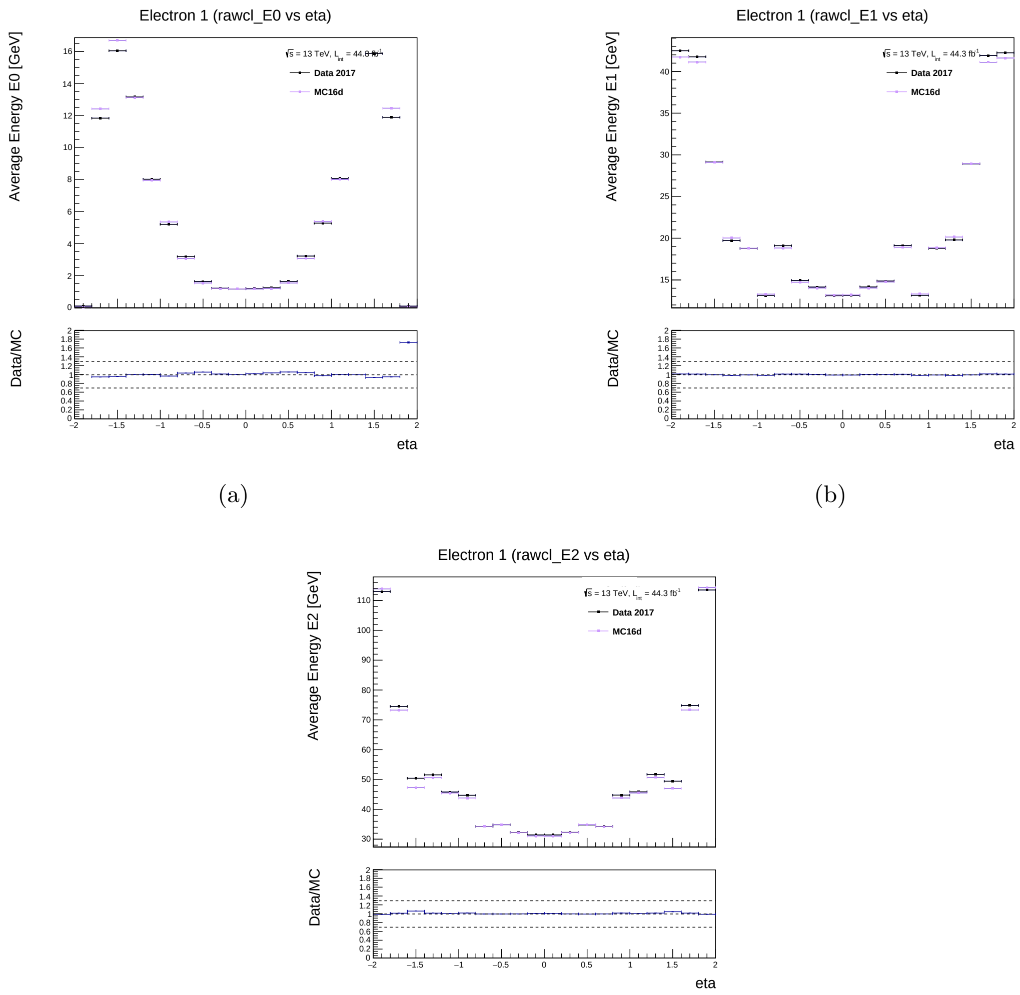

(a) (b) (c)

Figure 11: (a) Leading electron raw cluster energy distribution as a function of η in Layer 0 (b) Equivalent plot for layer 1 (c) Equivalent plot for layer 2.

By inspecting Figure 11, a good agreement between real data and simulated data can be observed for all layers.

5 Results

5.1 Overview

A description of the results of this study will be presented in this chapter. A comparison with results from a previous study will also be presented along with results obtained via muon analysis.

5.2 Presampler Scale using Electrons

To compute the PS scale (α_{PS}), the material correction ($E_0^{corr}(\eta)$) is computed first. Following equation 2.1, the computation is done by combining $E_{1/2}^{data}(\eta)/E_{1/2}^{nom}(\eta)$ (Figure 12), the upstream material correction factor (A(η)) (Table 4), the $E_{1/2}$ intercalibration correction factor ($b_{1/2}(\eta)$) (Section 2.4) and the MC energy deposits in the PS ($E_0^{nom}(\eta)$) (Figure 11(a)).

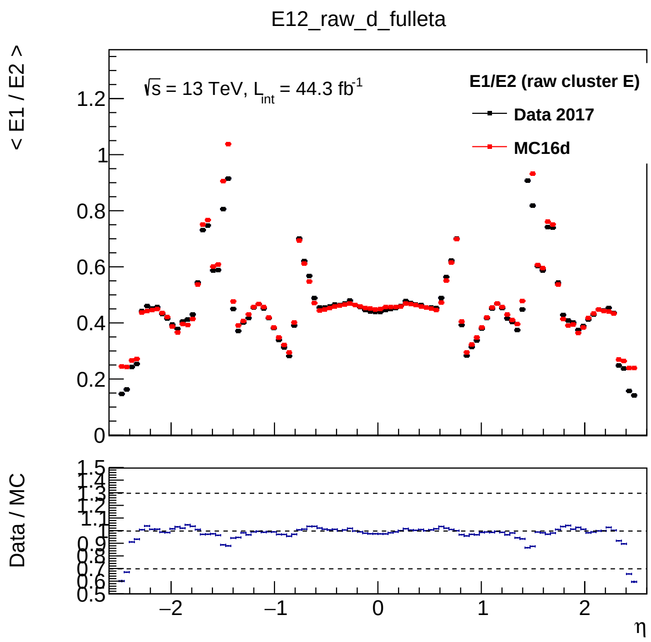

Figure 12: Ratio of raw cluster energies in layers 1 and 2 as a function of η.

Once $E_0^{corr}(\eta)$ is computed, the PS scale is computed following equation 2.2. This is done by dividing $E_0^{data}(\eta)$ (Figure 11(a)) by the material correction. It is also important to note that the PS scale is also computed using the corrected cluster energy distributions shown in Figure 13. This is done by following the same approach outlined earlier but working with Figure 13 instead of 11 and 12.

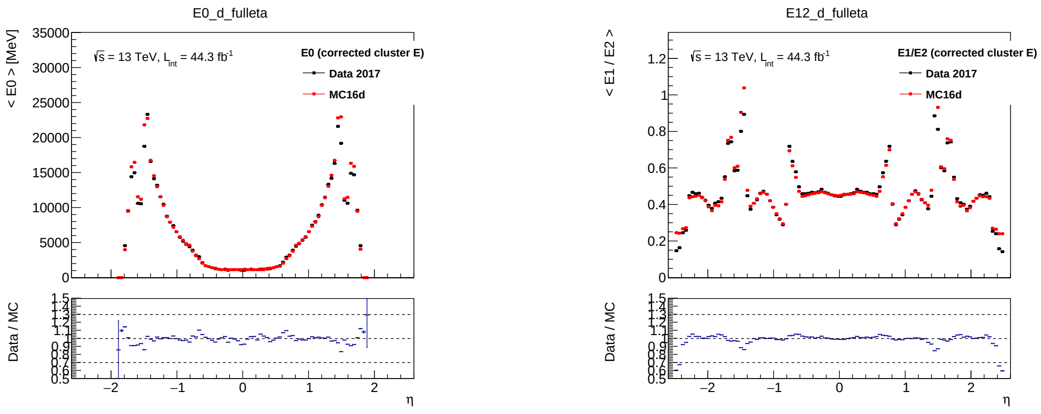

(a) (b)

Figure 13: (a) Leading electron corrected cluster energy distribution as a function of η in PS (b) Equivalent plot of the ratio of corrected cluster energies in layer 1 and layer 2.

At this stage, the PS scale results obtained in [8] were used as a reference since the results in that study were acquired using the same methodology while using data taken in 2018 during the full run-2 along with a different simulated MC sample. These results are shown in Figure 14 while the results of this study are shown in Figure 15.

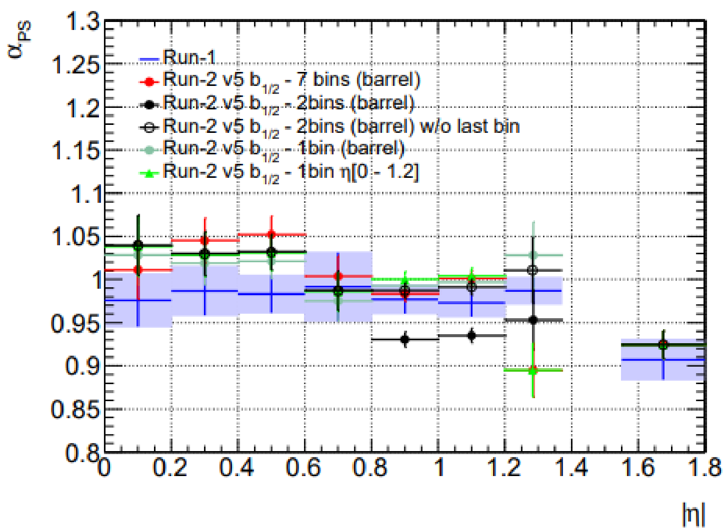

Figure 14: Presampler scale using electrons as extracted from [8].

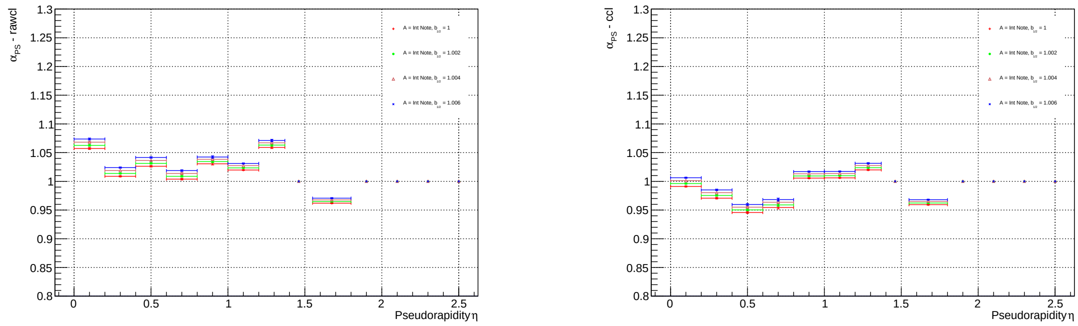

(a) (b)

Figure 15: (a) α_{PS} computed using raw cluster energies (b) Equivalent plot using corrected cluster energies. The associated errors were computed using standard error propagation techniques (See section 2.2.1).

By inspecting Figure 14, it is evident that the PS scale obtained in [8] is approximately equal to 1 for all η bins with the exception of $1.55 < |\eta| < 1.8$ bin which is closer to 0.9. Therefore, the distributions observed in Figure 15 (a) & (b) both being close to 1 is expected. Moreover, when comparing Figure 15 (a) & (b), a downshift of the PS scale is observed when it is computed using corrected cluster energies with again with the exception of $1.55 < |\eta| < 1.8$ bin.

As discussed in section 2.3, $A(\eta)$ is derived using MC samples with distorted geometries whilst $b_{1/2}(\eta)$ is derived from comparison of data and MC for photons, and this corrects material between presampler and layer 1 as well as residual data-MC differences in E1/E2 calibration. However, the relevant samples were not available (at the time of the study) and the PS scale was computed using correction factors from [8]. Due to the afforementioned, a fair comparison could not be made until the updated correction factors were obtained. For A(eta), the main reason why it could be slightly different for rel21 compared to 20.7 (2017 Internal Note [8]) is the change of the clustering algorithm to superclusters while $b_{1/2}(\eta)$ should also be derived with rel21 data instead of rel20.7. For a fair comparison to be made, the PS scale was re-computed using the same real data and MC samples using in [8]. The PS scale computed using 2018 Run-2 data and mc16e sample are shown in Figure 16. A close match between the PS scale derived using 2017 data and the one using 2018 data is observed upon comparing Figures 15 and 16, as expected.

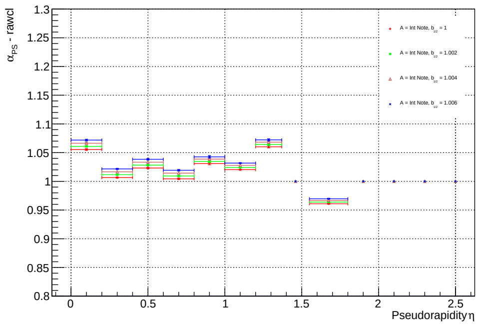

(a)

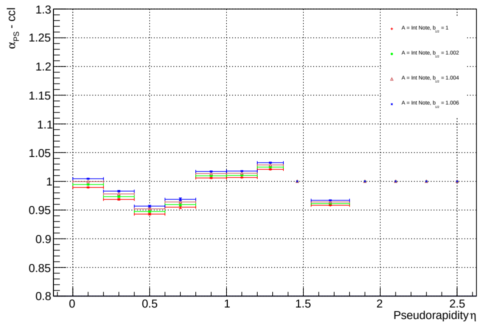

(b)

Figure 16: (a) α_{PS} computed using raw cluster energies (2018 data & mc16e) (b) Equivalent plot using corrected cluster energies. The associated errors were computed using standard error propagation techniques (See section 2.2.1).

5.3 Presampler Scale using Muons

To test the layer intecalibration and compute the presampler scale, muons are preferred over electrons because of their blindness to the amount of material in front of the calorimeter. However, measurements obtained with muons should be cross-checked with electrons to verify the validity of the results. This presampler energy scale calibration analysis using muons is discussed in [11]. In the particular study, muons from Z and W boson decays were used from 2017 and 2018 of the full LHC Run-2 data. It is also important to note that the study was performed using low-pileup (low-μ) data to ensure a good signal-to-noise ratio in comparison to the full Run-2 data.

According to Figure 17, the PS scale computed using muons from Z and W boson decays is in the range of 0.95 to 1 for all η bins which seems to be in agreement with the PS scale computed in this study (Figure 15 (b)). However, a fair comparison cannot be made since the updated correction factors have to be obtained.

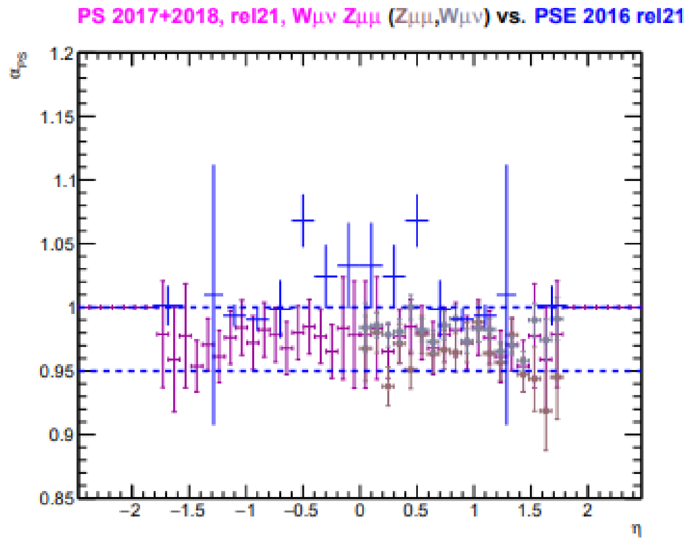

Figure 17: Presampler scale using muons as extracted from [11].

5.4 Impact of Correction Factors $\mathbf{b}_{1/2}(\eta)$ & $\mathbf{A}(\eta)$

Assessing the impact of the $\mathrm{b}_{1/2}(\eta)$ intercalibration correction factor was straight forward. By inspecting 15 (a) & (b), it is evident that the effect of this factor is to upshift (or downshift) the presampler scale. This is seen when the factor is set to 1.006 and the α_{PS} is shifted upwards compared to lower $\mathrm{b}_{1/2}(\eta)$ values. This behaviour is expected following equations 2.1 and 2.2. To investigate the impact of the upstream material correction factor $\mathrm{A}(\eta)$, the PS scale using electrons was computed with varied $\mathrm{A}(\eta)$. One of the tests involved an $\mathrm{A}(\eta)$ larger by a factor of 1.5 whereas the other test involved halving $\mathrm{A}(\eta)$.

1.5 × $\mathbf{A}(\eta)$

The new correction factor $\mathrm{A}(\eta)$ was set for each bin by multiplying the corresponding values in Table 4 by 1.5 and then computing the PS scale. The results using the modified correction factor are shown in Figure 18.

The impact of amplifying $\mathrm{A}(\eta)$ was assessed by comparing Figures 15 (a), 18 (a) and Figures 15 (b), 18 (b). The observations are summarised in Table 7.

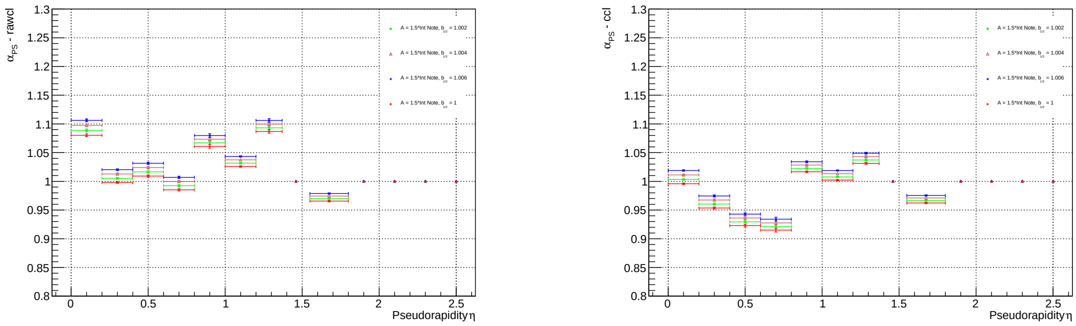

(a) (b)

Figure 18: (a) α_{PS} computed using raw cluster energies and amplified A(η) (b) Equivalent plot using corrected cluster energies. The associated errors were computed using standard error propagation techniques (See section 2.2.1).

Pseudorapidity Region	15(a) (a) vs 18(a)	15(b) vs 18(b)
$0 < \|\eta\| < 0.2$	+ 0.02	=
$0.2 < \|\eta\| < 0.4$	- 0.01	- 0.02
$0.4 < \|\eta\| < 0.6$	- 0.02	- 0.02
$0.4 < \|\eta\| < 0.8$	- 0.03	- 0.03
$0.8 < \|\eta\| < 1.0$	+ 0.03	+ 0.02
$1.0 < \|\eta\| < 1.2$	+ 0.01	- 0.01
$1.2 < \|\eta\| < 1.37$	+ 0.02	+ 0.02
$1.37 < \|\eta\| < 1.52$	-	-
$1.55 < \|\eta\| < 1.8$	+ 0.01	+ 0.01

Table 7: Summary of the deviations caused by the amplification of A(η). The differences were taken from the lowest distribution (red).

It is evident from Table 7 that altering A(η) is more complex than $b_{1/2}(\eta)$. However, it can be clearly deduced by comparing the relevant Figures that amplifying A(η) spreads the PS scale computed with different $b_{1/2}(\eta)$ values. This is expected from equation 2.1.

$0.5 \times \mathbf{A}(\eta)$

The new correction factor A(η) was set for each bin by multiplying the corresponding values in Table 4 by 0.5 and then computing the PS scale. The results using the modified correction factor are shown in Figure 19.

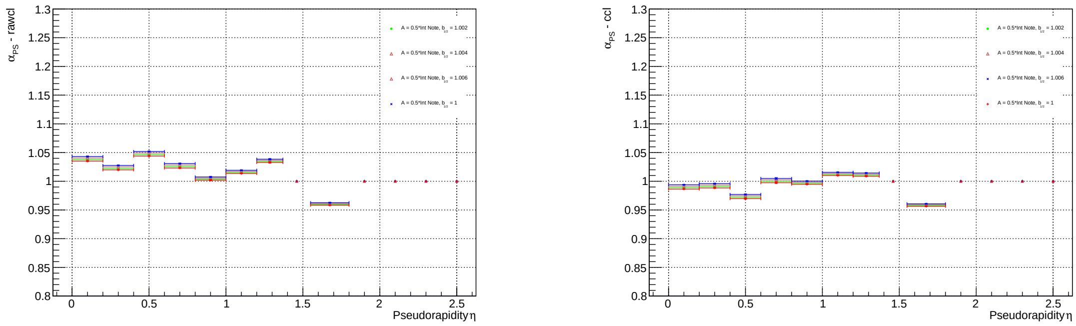

(a) (b)

Figure 19: (a) α_{PS} computed using raw cluster energies and halved A(η) (b) Equivalent plot using corrected cluster energies. The associated errors were computed using standard error propagation techniques (See section 2.2.1).

The impact of halving A(η) was assessed by comparing Figures 15 (a), 19 (a) and Figures 15 (b), 19 (b). The observations are summarised in Table 8.

Pseudorapidity Region	15(a) vs 19(a)	15(b) vs 19(b)
$0 < \|\eta\| < 0.2$	- 0.02	=
$0.2 < \|\eta\| < 0.4$	+ 0.01	+ 0.02
$0.4 < \|\eta\| < 0.6$	+ 0.02	+ 0.02
$0.4 < \|\eta\| < 0.8$	+ 0.03	+ 0.03
$0.8 < \|\eta\| < 1.0$	- 0.03	- 0.02
$1.0 < \|\eta\| < 1.2$	- 0.01	+ 0.01
$1.2 < \|\eta\| < 1.37$	- 0.03	- 0.01
$1.37 < \|\eta\| < 1.52$	-	-
$1.55 < \|\eta\| < 1.8$	- 0.01	- 0.01

Table 8: Summary of the deviations caused by the halving of A(η). The differences were taken from the lowest distribution (red).

The deviations observed in Table 8 are causing opposite shifts compared to those in Table 7 which is an expected outcome. In contrast to the case where A(η) was amplified, the PS scale results computed with different $b_{1/2}(\eta)$ values bunched when A(η) was halved which is once again expected from equation 2.1.

6 Conclusion

Rel 21 2017 data were used and the corresponding MC samples to derive the Presampler energy scale α_{PS}, and its associated uncertainties. The results are discussed in Section 5.2 and the statistical uncertainty propagation is discussed in Section 2.2.1.

In the future, the study could be improved by obtaining the updated correction parameters $A(\eta)$ and $b_{1/2}(\eta)$ using the relevant samples. This would enable a fair comparison between PS scale obtained in [8] using electrons as well as the one obtained in [11] using muons. Last but, not least the systematic uncertainties could be obtained to further improve the accuracy of the results.

7 Acknowledgements

To begin with, I would like to express my gratitude to Dr. Otilia Ducu for allowing me to undertake this study. It is amazing working amongst the ATLAS group. I am grateful for the experiences and the skills that I have acquired through this study. Working through the pandemic and communicating via Zoom/Skype was not an easy task but, I am honored for the opportunity. I would also like to thank Marteen and Guillame Unal for their previous work on the PS calibration. I would also like to thank Fabio for sharing the ntuples used in this study along with Ahmed for sharing the framework. Last but, not least, I am grateful for being able to present in the Egamma meetings and I would like to thank Stefano Manzoni and Yanping Huang for hosting them.

References

[1] Home.cern. 2021. Experiments | CERN. [online] Available at: <https://home.cern/science/experiments.

[2] CERN. 2021. ATLAS. [online] Available at: <https://home.cern/science/experiments/atlas>.

[3] Reed, R., 2015. The Upgrade of the ATLAS Tile Calorimeter Readout Electronics for Phase II. Journal of Physics: Conference Series, 623, p.012024.

[4] ATLAS Experiment at CERN. 2021. Detector & Technology. [online] Available at: <https://atlas.cern/discover/detector>.

[5] Aaboud, M. etal. 2016. Measurement of the photon identification efficiencies with the ATLAS detector using LHC Run-1 data. The European Physical Journal C, 76(12).

[6] Guo, B., 2011. Measurement of the Top Quark Pair Production Cross Section and an in-situ B-tagging efficiency Calibration with ATLAS in pp collisions at sqrts=7 TeV in Dilepton Final States

[7] Hubaut, F., 2004. Performance of the ATLAS electromagnetic calorimeter under beam tests. Nuclear Instruments and Methods in Physics Research Section A: Accelerators, Spectrometers, Detectors and Associated Equipment, 518(1-2), pp.31-35.

[8] Maarten Boonekamp, Lydia Iconomidou-Fayard, Oleh Kivernyk, Sandrine Laplace, Antoine Laudrain, Arthur Schaffer, Reisaburo Tanaka, Ahmed Tarek, Guillaume Unal, ,Electromagnetic calorimeter layers energy scale determination, ATL-COM-PHYS-2017-760, 2017, https://cds.cern.ch/record/2268812 (cit. on pp. 4, 8, 20, 37, 39).

[9] Zuzana Barnovska, Maarten Boonekamp, Marco Delmastro, Bruno Lenzi, Narei Lorenzo Martinez, Philippe Schwemling, Florian Teischinger, Guillaume Unal, Liwen Yao, Electromagnetic calorimeter layers energy scales determination, ATL-COM-PHYS-2013-1423, 2013, https://cds.cern.ch/record/1609068/files/ATL-COM-PHYS-2013-1423.pdf

[10] Opendata.atlas.cern. 2021. ATLAS events. GitBook. [online] Available at: <http://opendata.atlas.cern/books/current/get-started/book/atlasevents.html>.

[11] Otilia D. 2021. Presampler energy scale calibration using muons. https://cds.cern.ch/record/2268812

A Appendix

A.1 α_{PS} - 2017

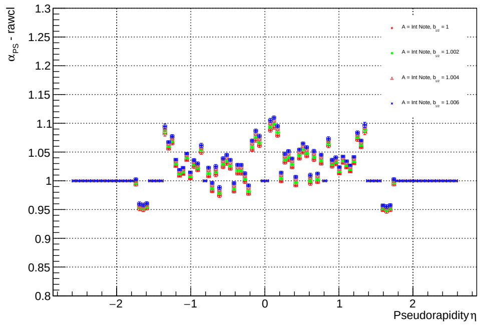

(a)

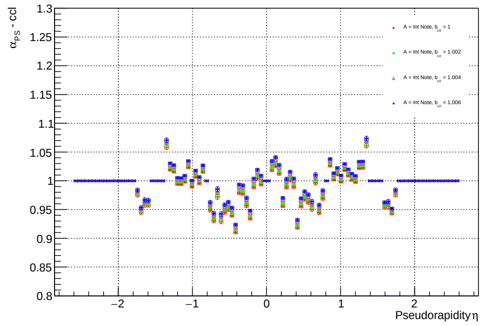

(b)

Figure 20: (a) α_{PS} computed using raw cluster energies (106 η bins) (b) Equivalent plot using corrected cluster energies. The associated errors were computed using standard error propagation techniques.

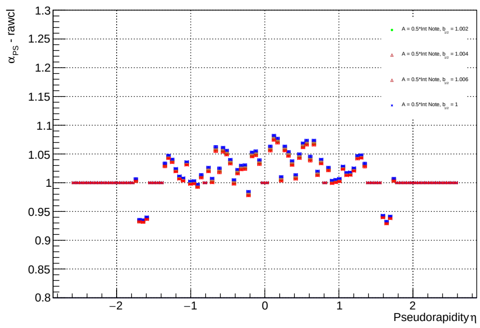

(a)

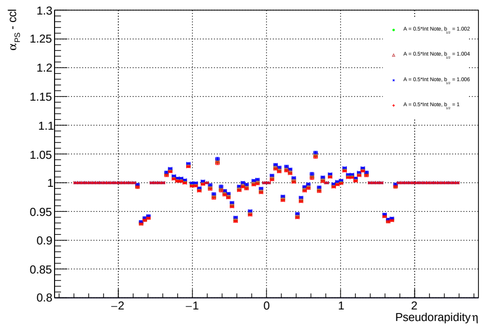

(b)

Figure 21: (a) α_{PS} computed using raw cluster energies (106 η bins) and halved A(η) (b) Equivalent plot using corrected cluster energies. The associated errors were computed using standard error propagation techniques.

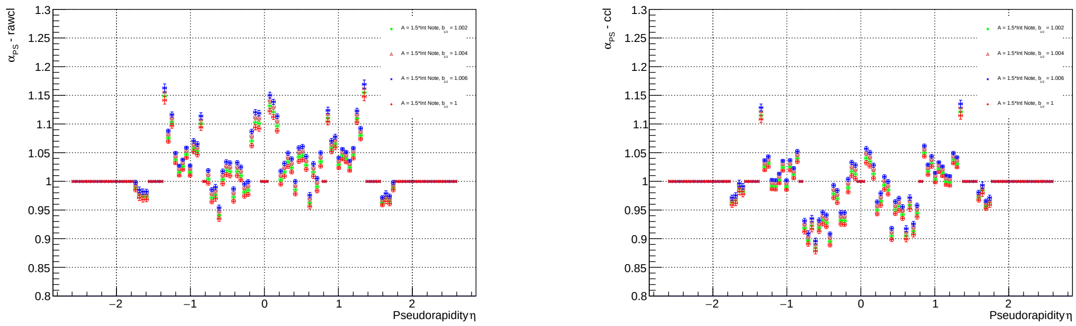

(a) (b)

Figure 22: (a) α_{PS} computed using raw cluster energies (106 η bins) and amplified A(η) (b) Equivalent plot using corrected cluster energies. The associated errors were computed using standard error propagation techniques.

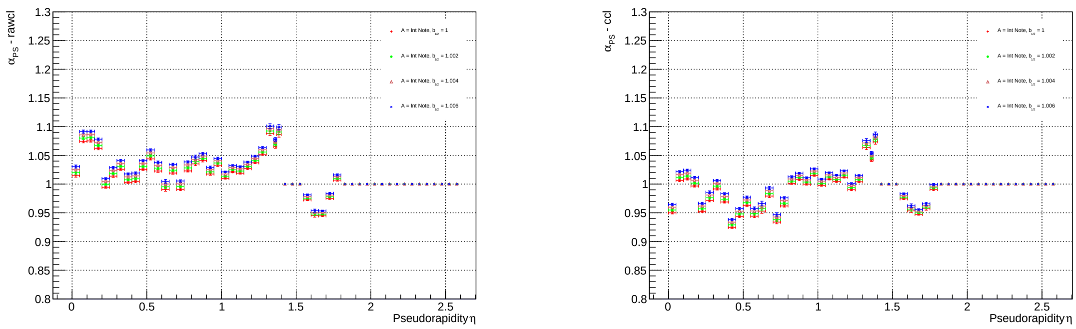

(a) (b)

Figure 23: (a) α_{PS} computed using raw cluster energies (53 η bins) (b) Equivalent plot using corrected cluster energies. The associated errors were computed using standard error propagation techniques.

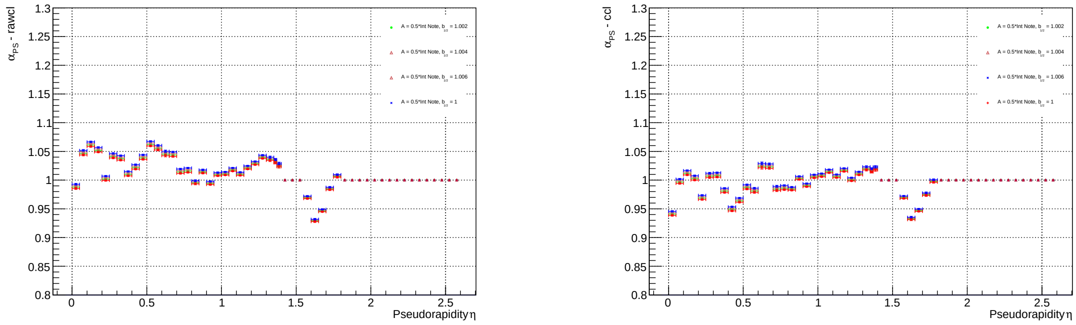

(a) (b)

Figure 24: (a) α_{PS} computed using raw cluster energies (53 η bins) and halved A(η) (b) Equivalent plot using corrected cluster energies. The associated errors were computed using standard error propagation techniques.

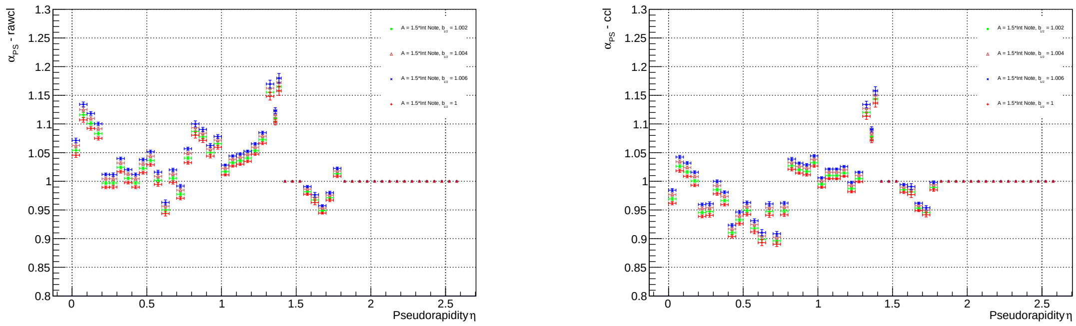

(a) (b)

Figure 25: (a) α_{PS} computed using raw cluster energies (53 η bins) and amplified A(η) (b) Equivalent plot using corrected cluster energies. The associated errors were computed using standard error propagation techniques.

A.2 α_{PS} - 2018

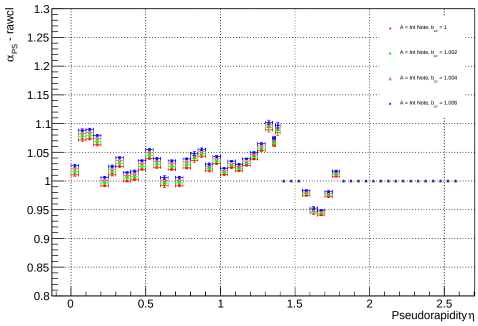

(a)

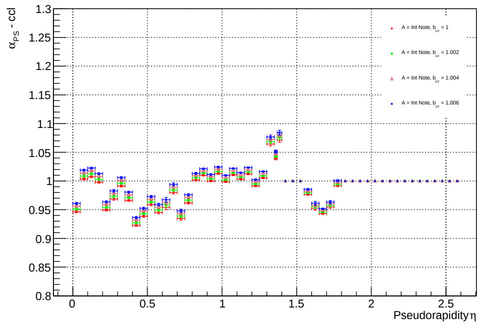

(b)

Figure 26: (a) α_{PS} computed using raw cluster energies (53 η bins) (b) Equivalent plot using corrected cluster energies. The associated errors were computed using standard error propagation techniques.

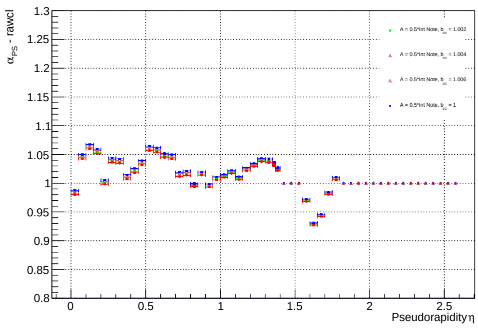

(a)

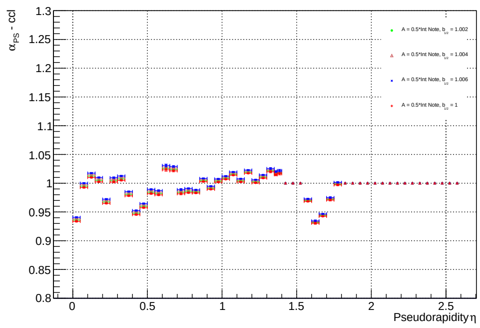

(b)

Figure 27: (a) α_{PS} computed using raw cluster energies (53 η bins) and halved A(η) (b) Equivalent plot using corrected cluster energies. The associated errors were computed using standard error propagation techniques.

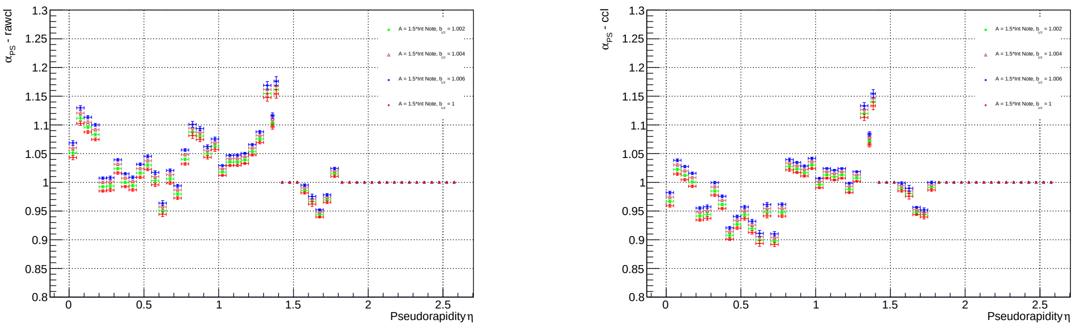

(a) (b)

Figure 28: (a) α_{PS} computed using raw cluster energies (53 η bins) and amplified A(η) (b) Equivalent plot using corrected cluster energies. The associated errors were computed using standard error propagation techniques.